Soft Matter

High-resolution structure of coexisting nanoscopic and microscopic lipid domains†

Michal Belička,*[ab] Anna Weitzer[ab] and Georg Pabst*[ab]

We studied coexisting micro- and nanoscopic liquid-ordered/liquid-disordered domains in fully hydrated multilamellar vesicles using small-angle X-ray scattering. Large domains exhibited long-range out-of-plane positional correlations of like domains, consistent with previous reports. In contrast, such correlations were absent in nanoscopic domains. Advancing a global analysis of the *in situ* data allowed us to gain a deep insight into the structural and elastic properties of the coexisting domains, including the partitioning of cholesterol in each domain. In agreement with a previous report, we found that the thickness mismatch between ordered and disordered domains decreased for nanoscopic domains. At the same time, we found also the lipid packing mismatch to be decreased for nano-domains, mainly due to the liquid-disordered domains becoming more densely packed when decreasing their size.

1 Introduction

Biological membranes are well-known to define and control intra- and intercellular environments. One of the most intriguing features of biomembranes is their lateral heterogeneity,[1–3] called domains or rafts,[4] which have been postulated to be involved in a wide range of physiological processes.[5,6] Efforts to provide direct experimental evidence for the existence of membrane rafts have not been without significant controversy,[7,8] which is often attributed to their small, nanoscopic size and/or short life-times.[9]

In contrast, membrane domains are well-established in complex lipid-only mixtures of low- and high-melting lipids and cholesterol (Chol),[10] or other sterols which are able to condense saturated hydrocarbons.[11,12] Lipid-only domains of so-called liquid ordered (L_O) and liquid disordered (L_D) phases have been studied by a wide range of experimental techniques, including fluorescence microscopy (see, *e.g.*, ref. 13), Förster resonance energy transfer (FRET) (see, *e.g.*, ref. 14), neutron diffraction,[15] small-angle X-ray and neutron scattering (SAXS, SANS),[16] or nuclear magnetic resonance (see, *e.g.*, ref. 17). L_O domains are considered as archetypes of rafts and their structural and elastic properties are of particular interest for understanding selective protein partitioning.[18,19]

One of the interesting features of cholesterol-containing raft-like lipid mixtures is the ability to control domain size by lipid composition.[20] For example, ternary mixtures with diunsaturated or highly branched lipids as the low-melting component display micron-sized domains, which can be readily observed under a microscope using fluorescent lipid labels (see, *e.g.*, ref. 21). Exchanging the diunsaturated lipids to monounsaturated lipids, like palmitoyloleoylphosphocholine (POPC), instead reduces the size of these domains to a few nanometers.[14,22–24] Alternatively, such systems have been proposed to resemble a microemulsion.[25] Deciphering the intrinsic structural properties of nanoscopic L_O/L_D domains is highly challenging. Most recently, Nickels and coworkers[26] were able to describe the thickness and bending rigidity of coexisting L_O and L_D domains in the nanoscopic regime in large unilamellar vesicles (LUVs) applying neutron scattering in combination with contrast variation.

Here, we set out to show that detailed structural and elastic information of nanoscopic lipid domains in multilamellar vesicles (MLVs) can be retrieved from a global SAXS data analysis. Besides domain thickness and thickness of the hydrocarbon chain layer, our analysis is capable of retrieving the maximum bending fluctuation amplitudes of domains, as well as the packing density of lipids and the partitioning of cholesterol in L_O/L_D domains.

To achieve this goal, we followed the approach of Heftberger *et al.*,[27] who detailed the analysis of coexisting micron-sized domains in MLVs by combining a modified Caillé theory description of the structure factor,[28] with a scattering length density profile (SDP) model[29] for the form factor. Our modeling led us also to reconsider domain stacking in the microscopic and nanoscopic regimes allowing for contributions of partially anticorrelated domains and overlapping domain leaflets. Additional modifications of our previous modeling included an intrinsic definition of the area per lipid (area per unit cell) and a generic

[a] *University of Graz, Institute of Molecular Biosciences, Biophysics Division,*
NAWI Graz, Humboldtstr. 50/III, A-8010 Graz, Austria.
E-mail: michal.belicka@uni-graz.at, georg.pabst@uni-graz.at
[b] *BioTechMed-Graz, A-8010 Graz, Austria*
† Electronic supplementary information (ESI) available. See DOI: 10.1039/c6sm02727j

parameterization of cholesterol distribution within the coexisting domains, which allows to extract cholesterol partitioning with high fidelity. Our SDP model for cholesterol differs from previous descriptions[27,30] and is applicable for any other additive molecule(s) displaying affinity to either the L_D or L_O phase. The new model yielded improved results for high-resolution SAXS data on micron-sized domains and gave first insights on the structural properties of L_D and L_O domains in the nanoscopic regime. Most interestingly, we found that the previously reported decrease of the L_O/L_D thickness mismatch for nanoscopic domains[22] goes hand in hand with a decrease of the lipid packing mismatch.

2 Theory

Following the approach of Heftberger et al.[27,31] we adopted the global analysis model of Pabst et al.[32,33] to the case of coexisting domains. For completeness and clarity of arguments, we revisit some of the most important arguments leading to an improved model that also captures nanoscopic domains.

MLVs displaying coexisting domains were considered as stacks of weakly bound bilayers averaged over all possible spatial orientations. Micron-sized domains were shown to exhibit long-range alignment of like domains in the stacking direction (see, e.g., ref. 30, 34 and 35), giving rise to two distinct families of lamellar Bragg lattices, which we consider to be dominated by either L_O or L_D domains. That is, unlike previous assumptions, we presently also consider contributions from positionally anticorrelated domains, i.e., L_O in L_D and vice versa (Fig. 1a). The total scattering of such systems is

$$I_{tot}(q) \approx l_D \cdot I_D(q) + l_O \cdot I_O(q), \qquad (1)$$

where l_D and l_O are the volume fractions occupied by the L_D phase and the L_O phase 'dominated' stacks ($l_D + l_O = 1$), respectively, $I_{D,O}(q)$ are the scattering intensities of the respective stacks, and q is the modulus of transferred momentum.

For nanoscopic domains, only a single lamellar lattice is observed (see the Results section). That is, $I_{tot}(q)$ contains contributions from L_O and L_D domains, but unlike MLVs with micron-sized domains, the interbilayer separation between L_O and L_D domains is identical (Fig. 1b).

Assuming that the fluctuations within the bilayer are independent of the fluctuations of the lattice points, the scattered intensities of MLVs can be split according to Debye into the structure factor $S(q)$, describing the dynamic positional correlations between the layers and the form factor $F(q)$, which accounts for the transbilayer/domain structure.[36] Thus, for scattering from a stack consisting of N positionally correlated bilayers in either the micro- or nanoscopic regime,

$$I^{corr}(q) = \frac{1}{q^2}\big[S(q) \cdot |\langle F(q)\rangle|^2 + N \cdot \big(\langle|F(q)|^2\rangle - |\langle F(q)\rangle|^2\big)\big],$$
$$(2)$$

where $\langle \cdots \rangle$ represents averaging through all bilayers within a given stack.
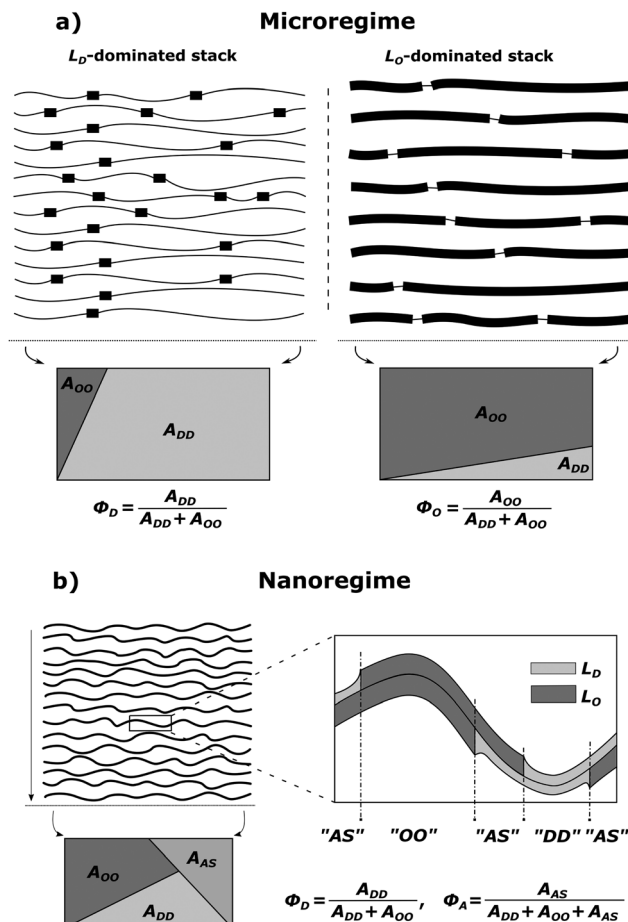

Fig. 1 Schematic of domain alignment in the microscopic (a) and the nanoscopic regimes (b) in MLVs. L_D domains are represented by thin and L_O domains by thick lines, respectively. In the microscopic regime, each stack is dominated by either L_D or L_O domains, but also contains contributions from unlike domains. Such impurities are taken into account by the purity parameters, Φ_D and Φ_O, which are based on the surface area fractions of liquid ordered A_{OO} and liquid disordered A_{DD} domains (see also eqn (15)–(18)). The rectangles give a graphical representation of the irradiated surface area within a scattering volume element, which is divided into individual fractions. In the nanoscopic regime, an additional area fraction of leaflet anticorrelated domains A_{AS} needs to be taken into account in the purity parameter Φ_D (see text for details).

Additional scattering contributions from positionally uncorrelated bilayers/domains, originating, e.g., from defects due to packing mismatches, need to be considered.[33] Taking these into account, the full scattering intensity of each stack becomes

$$I_s(q) = \frac{1}{q^2}\big[(1 - f_{diff})I^{corr}(q) + f_{diff}|\langle F(q)\rangle|^2\big], \qquad (3)$$

where f_{diff} gives the fraction due to diffuse scattering. Naturally, f_{diff} comprises also of the scattering contributions from unilamellar vesicles, that may be present in the sample.

2.1 Structure factor

Positional correlations of fluid multibilayers are known to be affected by membrane undulations, which can be described by

the modified Caillé theory (MCT).[28,37] Within this theory the structure factor for each stack is

$$S_{MCT}(q; N) = N + 2 \sum_{k=1}^{N-1} \{ (N-k) \cos(kqd) \quad (4)$$
$$\times \exp(-(d/2\pi)^2 q^2 \eta [\gamma + \ln(\pi k)]) \},$$

where N is the number of spatially correlated bilayers per scattering domain, γ is Euler's constant and

$$\eta = \frac{\pi k_B T}{2d^2 \sqrt{K_C B}} \quad (5)$$

is the Caillé parameter, which is a measure of bilayer fluctuations, that depend on temperature T, the bending rigidity K_C and the bulk modulus of the interbilayer interactions, B (k_B is Boltzmann's constant).[38] From η we can directly calculate the fluctuations in bilayer separation $\Delta_{fl}^2 = \eta d^2/\pi^2$.[39] The polydispersity of N can be described by different probability distributions.[28,37,39,40] Here we chose an exponential probability distribution

$$f(N; N_{mean}) = \frac{1}{N_{mean}} \exp\left(-\frac{N}{N_{mean}}\right), \quad (6)$$

which is a special case of the well-known Schulz–Flory distribution,[41–43] where N_{mean} is the sample average of N. We also tested a regular Schulz–Flory distribution, but the exponential distribution yielded better fits for all the presently studied systems.

2.2 Form factor

To model the form factor, we have to consider two different scenarios (Fig. 1): (i) leaflet-correlated domains (L_O/L_O, L_D/L_D) and (ii) leaflet-anticorrelated domains (L_O/L_D, L_D/L_O). Micron-sized domains are well-known to exhibit transbilayer coupling of like domains.[44] Thus, only leaflet-correlated domains need to be considered. In the nanoscopic regime, both types of domains may occur as suggested by a recent simulation study.[45] In general, the form factor is given by the Fourier transformation of the contrast scattering length density profile $\Delta\rho(z)$ ($=\rho(z) - \rho_s$) along the bilayer normal, z,

$$F(q) = \int_{-d/2}^{d/2} \Delta\rho(z) e^{-iqz} dz, \quad (7)$$

where $\rho(z)$ is the transbilayer electron density and ρ_s is the electron density of the solvent. Note that leaflet-correlated domains represent a centrosymmetric crystalline system, while leaflet-anticorrelated domains are asymmetric.

In order to easily differentiate between symmetric and asymmetric systems, we describe the transdomain structure for each leaflet separately. For modeling the internal leaflet structure, we applied the scattering length density profile (SDP) description developed by Kučerka et al.,[29,46] which allows to jointly analyze X-ray and neutron scattering data. In the framework of the SDP model, each lipid molecule is parsed into quasi-molecular fragments. For the presently studied lipids, these components are the choline methyl groups (ChoMet), phosphate + CH$_2$CH$_2$N (PCN), glycerol + carbonyls (GC),

hydrocarbon methylene groups (HC) and finally the terminal chain methyls (CH$_3$).

The crystallographic unit cell is therefore realized by a single phospholipid molecule, which is in the present experimental case given by an averaged DSPC/DOPC, or DSPC/POPC molecule. Cholesterol is considered as an additive, which is able to distribute into L_D and L_O phases as discussed in Section 2.3. The base area of this unit cell is an important structural parameter – the interfacial area per lipid molecule A. In the case of lipid mixtures with cholesterol, A also contains a fraction of cholesterol and is therefore referred to as the area per unit cell.[47] Naturally this applies to any admixture molecule. Note that this definition differs from the partial lipid areas reported in other studies.[48,49] Each individual component of the lipid molecule is represented in the SDP model by its lateral unit fraction $a_i(z)$ – a function describing the fractional contribution of a given component to A, requiring that $\sum_i a_i(z) \equiv 1$ due to ideal volume filling.

For each leaflet, the contribution of the hydrocarbon chain fraction is described by a single plateau-function

$$a_{HC}(z) = 0.5 \left[\text{erf}\left(\frac{z}{\sqrt{2}\sigma_C}\right) - \text{erf}\left(\frac{z - D_C}{\sqrt{2}\sigma_C}\right) \right], \quad (8)$$

where D_C and σ_C are the position and "roughness" of the hydrocarbon chain region interface, respectively, and erf(x) refers to the error function. In our SDP model, the HC volume V_C contains also a fraction of lipophilic additives,

$$V_C = V_{chains} + \sum_i r_i \cdot V_{adm,i}, \quad (9)$$

where V_{chains} is the total volume of the phospholipid hydrocarbon chains (i.e. a mixture of low-melting and high-melting lipids, excluding carbonyl groups), and $V_{adm,i}$ is the volume of the ith lipophilic additive, here given by cholesterol, added with a relative molar ratio of r_i. The calculation of r_i for L_O and L_D domains is detailed in Section 2.3. Because of the assumed conservation of volumes, D_C is coupled to A through

$$A = \frac{V_C}{D_C}. \quad (10)$$

Thus A and D_C are interdependent parameters. In the present work, we fitted A and derived D_C through eqn (10).

All other quasi-molecular fragments of the unit lipid molecule, i.e., the polar headgroup components and the terminal methyl group, are given by Gaussian probability densities[29] with an average volume distribution

$$v_i(z) = \frac{V_i}{\sqrt{2\pi}\sigma_i} \exp\left(-\frac{(z - z_i)^2}{2\sigma_i^2}\right), \quad (11)$$

where V_i is the molecular volume of the ith component (i = PCN, CG,...), z_i is the center of mass, and σ_i is the Gaussian standard deviation. Note that V_i needs to be scaled by its relative molar ratio r_i according to the concentration of cholesterol (or any admixture molecule in general), $V_i = r_i \cdot V_{i,single}$, where $V_{i,single}$

are the volumes reported for the pure lipid components. The corresponding $a_i(z)$'s are then given by

$$a_i(z) = \frac{v_i(z)}{A}. \tag{12}$$

The final transbilayer SDP is constructed by a step-by-step replacement of the homogeneous water (ρ_w)/hydrocarbon core (ρ_{HC}) background in both leaflets by properly scaled individual components (using eqn (12))

$$\rho(z) = \rho_w + \sum_{m \text{ in water}} a_m(z)(\rho_m - \rho_w) + \sum_{k \text{ in HC}} a_k(z)(\rho_k - \rho_{HC}), \tag{13}$$

where $\rho_{m,k} = n^e_{m,k}/V_{m,k}$ are the electron densities of a given quasi-molecular fragment with $n^e_{m,k}$ number of total electrons, and $\rho_{HC} = \rho_{CH_2}$. The first sum in eqn (13) runs through all components within the water environment (including the hydrocarbon chains core) and the second one through all hydrophobic components (e.g., terminal methyl groups, cholesterol). Because of minute differences in hydrocarbon volumes of the phospholipids studied here, we were not able to deconvolute their contributions. Therefore, the molecular averages of phospholipids in each domain were calculated according to reported compositional phase diagrams.[14,24] Since lipid headgroup volumes do not change significantly with temperature or phase,[50] the volumes and widths of the PC headgroup components were assumed to be the same in both phases. Their values were adopted from the works of Klauda et al.[51] and Kučerka et al.[46] The chain methylenes and methines carry insufficient electron density contrast to be detected by X-rays. We therefore fixed the hydrocarbon chain core widths and coupled their border positions (D_C) to the CG group $z_{CG} = D_C + 0.9$ Å using the values obtained by Kučerka et al.[46]

The hydrocarbon chain volumes were calculated using the data reported in ref. 50 and 52, assuming that

$$\frac{V_{CH}(L_O)}{V_{CH_2}(L_O)} = \frac{V_{CH}(L_D)}{V_{CH_2}(L_D)}, \tag{14}$$

and that $V_{CH_2}(L_O)$ equals the value reported for the gel phase (see Table S2 in the ESI†). Further, we assumed $V_{CH_3} = 2V_{CH_2}$ in the L_D-phase,[50] while V_{CH_3} was an adjustable parameter in the L_O domains.

In order to describe the scattering of microscopic or nanoscopic domains in MLVs, we now need to consider contributions from 'impurities'. In the case of micron-sized domains, these originate from unlike domains such as L_O in L_D dominated stacks and vice versa (Fig. 1a). The average area fraction of each domain in each stack is described by the purity Φ_i (Φ_D, Φ_O). For definition, see Fig. 1. The amplitudes of the averaged form factors and their averaged squared amplitudes in eqn (2) and (3) then become

$$|\langle F^D(q)\rangle| = |\Phi_D F_D(q) + (1 - \Phi_D)F_O(q)|,$$
$$|\langle F^O(q)\rangle| = |\Phi_O F_O(q) + (1 - \Phi_O)F_D(q)|, \tag{15}$$

and

$$\langle |F^D(q)|^2\rangle = \Phi_D|F_D(q)|^2 + (1 - \Phi_D)|F_O(q)|^2,$$

$$\langle |F^O(q)|^2\rangle = \Phi_O|F_O(q)|^2 + (1 - \Phi_O)|F_D(q)|^2. \tag{16}$$

In the case of nanoscopic domains, we do not find long-range alignment of like domains (see Section 4.2), but need to consider contributions from leaflet-anticorrelated domains (Fig. 1b). Thus, we have scattering from symmetric (L_O/L_O, L_D/L_D) and asymmetric domains (L_O/L_D, L_D/L_O). Since we have no measure for the orientation of the asymmetric domains, we assume that half of the asymmetric domains are L_O/L_D and the other half L_D/L_O. Defining the area fraction of asymmetric domains, Φ_A, as illustrated in Fig. 1b, we find the form factor amplitudes of nanoscopic domains

$$|\langle F^{nn}(q)\rangle| = |\Phi_A F_A(q) + (1 - \Phi_A)(\Phi_D F_D(q) + (1 - \Phi_D)F_O)| \tag{17}$$

and

$$\langle |F^{nn}(q)|^2\rangle = \Phi_A|F_A(q)|^2 + (1 - \Phi_A)(\Phi_D|F_D(q)|^2 + (1 - \Phi_D)|F_O(q)|^2), \tag{18}$$

where $F_D(q)$, and $F_O(q)$ are the form factors of symmetric L_D or L_O domains, respectively, and $F_A(q)$ is the form factor of asymmetric domains.

2.3 Partitioning of cholesterol

The effect of cholesterol (and any other added lipophilic molecule) on the scattering curve depends not only on the overall surface coverage of a given domain, but even more crucially on its molar ratio/fraction within L_O or L_D. Thus, the cholesterol content of a given domain can be determined from scattering experiments. Recently, Ma et al.[53] estimated cholesterol partitioning in L_D/L_O domains by fitting Gaussian-like functions to electron density profiles, assuming that the observed profile changes originate only from the added electron densities of cholesterol.

Here, we introduce an alternative approach, which does not rely on the above mentioned assumption. The relative molar ratios of cholesterol in L_D and L_O domains (r_D, r_O) can be decoupled from the overall molar ratio of cholesterol in the lipid mixture $r_{tot} = n_{chol}/n_{lip}$, where n_{chol} and n_{lip} are the total molar numbers of cholesterol and phospholipid per sample, by considering

$$r_{tot} = \frac{n_{lip,D} \cdot r_D + n_{lip,O} \cdot r_O}{n_{lip,D} + n_{lip,O}}, \tag{19}$$

with

$$n_{lip,D} = N_D \frac{l_D \Phi_D}{A_D} A_{ir} + N_O \frac{(1 - l_D)(1 - \Phi_O)}{A_D} A_{ir}, \tag{20}$$

$$n_{lip,O} = N_D \frac{l_D(1 - \Phi_D)}{A_O} A_{ir} + N_O \frac{(1 - l_D)\Phi_O}{A_O} A_{ir} \tag{21}$$

in the microscopic regime (see eqn (1) for the definition of l_D) and

$$n_{lip,D} = N \frac{0.5 \cdot \Phi_A + (1 - \Phi_A)\Phi_D}{A_D} A_{ir}, \tag{22}$$

$$n_{lip,O} = N \frac{0.5 \cdot \Phi_A + (1 - \Phi_A)(1 - \Phi_D)}{A_O} A_{ir} \tag{23}$$

in the nanoscopic regime. Here, A_{ir} is the average irradiated surface area of a single sheet within a given stack of bilayers, A_D/A_O are the

areas of the unit cells in the L_D/L_O domains, and N_D/N_O are the average numbers of positionally correlated bilayers in each stack.

Inserting eqn (20) into eqn (19) and eqn (22) into eqn (21) allows A_{ir} to be removed and one obtains after some arithmetic

$$r_O = r_{tot} + (r_{tot} - r_D)\cdot\Gamma, \tag{24}$$

where

$$\Gamma = \frac{N_D l_D \Phi_D + N_O (1 - l_D)(1 - \Phi_O)}{N_D l_D (1 - \Phi_D) + N_O (1 - l_D)\Phi_O} \cdot \frac{A_O}{A_D}, \tag{25}$$

for the microscopic regime and

$$\Gamma = \frac{0.5\Phi_A + (1 - \Phi_A)\Phi_D}{0.5\Phi_A + (1 - \Phi_A)(1 - \Phi_D)} \cdot \frac{A_O}{A_D}, \tag{26}$$

for the nanoscopic regime, which were used to evaluate eqn (9). Specifically, we fitted r_D and calculated r_O using the equations above. Heftberger et al.[27] used a similar model, but fitted r_D and r_O independently.

The molecular volume of cholesterol in L_D domains $V_{Chol}(L_D) = 628$ Å^3 was supplied from volumetric measurements of DOPC/Chol mixtures.[54] In turn, V_{Chol} is not known for L_O domains. We therefore decided to vary $V_{Chol}(L_O)$ between its known extremes in binary mixtures.[50] In most cases, the final value of $V_{Chol}(L_O)$ ended up between 600 Å^3 and 650 Å^3.

In each domain, cholesterol is parsed into a head and acyl tail group.[55] We further assumed that the electron density of the acyl tail group $\rho_{Chol}^t = \rho_{HC}$, from which we calculate the corresponding volume $V_{Chol}^t = n_e^t/\rho_{Chol}$, with n_e^t being the number of electrons of the cholesterol tail. The cholesterol head group volume is simply derived from $V_{Chol} = V_{Chol}^h + V_{Chol}^t$. The cholesterol head group is represented by a Gaussian-like $a_{Chol}(z)$ (12).

2.4 Domain thickness

For comparison to other structural data, we define the Luzzati thickness as a measure for the thickness of the domains as[56]

$$D_B = 2\frac{V_L + r_i \cdot V_{adm}}{A}, \tag{27}$$

where V_L and V_{adm} are the total volumes of the mixed phospholipid molecule and the admixture molecule (here cholesterol), respectively, and r_i is the relative molar ratio of the admixture in a given domain. Alternatively, the head-to-head distance of a given domain is defined as the cross-bilayer distance between the PCN groups

$$D_{HH} = 2z_{PCN}. \tag{28}$$

3 Materials and methods

3.1 Chemicals

POPC, DOPC and DSPC were purchased from Avanti Polar Lipids (Alabaster, AL, USA) and cholesterol from Sigma-Aldrich (Vienna, Austria) as dry powders. All lipids were used without any further purification. Organic solvents of spectral purity were obtained from Lactan (Graz, Austria) and Milli-Q water (18 MΩ cm at 25 °C) was freshly prepared before use.

3.2 Sample preparation

Dispersions of fully hydrated MLVs were prepared by rapid solvent exchange (RSE) as detailed by Rieder et al.[57] Briefly, first stock solutions were prepared by dissolving weighted amounts of lipid in a methanol/chloroform (1/9) solvent. Lipid concentration was determined to <1% by inorganic phosphate assay.[58] Lipid mixtures of POPC:DSPC:Chol = 0.39:0.39:0.22 and DOPC:DSPC:Chol = 0.46:0.3:0.24 were obtained by mixing appropriate amounts of the stock solutions. Then 300 μl of each solution was transferred into a test tube containing 600 μl Milli-Q water using a gastight Hamilton syringe. The test tube was mounted onto the RSE apparatus and heated under a constant stream of argon to 70 °C (above the boiling points of methanol and chloroform). This allowed fast evaporation of the organic solvent without the need of negative pressure. Each mixture was evaporated for 12 minutes. During evaporation, samples were constantly vortex-mixed at 1000 rpm to prevent sedimentation of methanol–chloroform solution droplets as well as to increase their evaporation rate. The final lipid concentration in each sample was at least 30 mg ml^{-1}.

3.3 Measurements

The SAXS scattering curves were obtained either at the ESRF BM29 BioSAXS beamline[59] (Grenoble, France) or at the P12 SAXS beamline[60] at DESY (Hamburg, Germany). At BM29, the samples were measured at an X-ray wavelength of $\lambda = 0.99$ Å using a sample-detector distance (SDD) of 2.869 m, whereas the experiments at the P12 beamline were performed at $\lambda = 0.6$ Å and SDD = 3.1 m. Scattered intensities were recorded using a Pilatus 1M (BM29), or a Pilatus 2M (P12) detector (Dectris, Baden, Switzerland).

At both beamlines, the samples were transferred prior to measurement into multi-well plates and equilibrated for 10 minutes in a temperature-controlled block. An automated sample robot delivered 20–35 μl of the lipid sample into a preheated glass capillary. For each sample, 20 frames were recorded with an exposure time of 0.095 s at P12 and 10 frames, each with 1 s exposure, at BM29. Water background was measured before and after each sample. To avoid introductions of artifacts by radiation damage, the data collected in subsequent frames were compared and rejected in case of statistically significant deviations. Background subtraction was performed by using the ATSAS software suite.[61]

3.4 Model evaluation

The final form of the model function for the microscopic regime is

$$I_{tot}(q) = K\cdot(l_D\cdot I_{d,diff}(q) + (1 - l_D)\cdot I_{o,diff}(q)) + I_{bckg} \tag{29}$$

and for the nanoscopic regime

$$I_{tot}(q) = K\cdot I_{nn,diff}(q) + I_{bckg}, \tag{30}$$

where K is a scaling constant and I_{bckg} is the flat background intensity originating from incoherent scattering. The fitting was achieved by minimizing

$$\chi^2 = \sum_i \frac{(I_{exp,i} - I_{tot}(q_i))^2}{\Delta I_{exp,i}^2}, \tag{31}$$

where $I_{\exp,i}$ are the measured intensities and $\Delta I_{\exp,i}$ their uncertainties. The overall large number of model parameters bear the potential of over-fitting, which needs to be addressed carefully. Our strategy was to fix or constrain as many parameters as possible using data from previous scattering studies applying a SDP analysis and complementary techniques, such as dilatometry. In particular, we fixed (i) the widths and (ii) the relative positions of all headgroup Gaussians (PCN, ChoMet) with respect to the GC-group, using values obtained by Kučerka et al.[46] and (iii) set the distance between the GC-group and the water-chains interface (z_{CG}–D_C) to 0.9 Å, capturing its reported range of 0.8–1 Å.[46] Further details of the used parameters and the underlying assumptions were discussed in the previous section. All parameters supplied from previous measurements are summarized in Table S2 (ESI†).

The remaining overall number of adjustable parameters varied between 18 in the microscopic regime and 13 in the nanoscopic one. The application of a global search algorithm was therefore necessary in order to avoid getting stuck in a local minimum during optimization. More specifically, optimization was carried out by the combination of the differential evolution algorithm[62] and the minimization and error analysis library MINUIT2 (CERN Program Library entry D506, utilizing the Levenberg–Marquardt algorithm).

4 Results and discussion

Prior to applying our model to coexisting domains, we tested its capabilities on well-studied single component bilayers of pure DOPC. Our best fit agreed well with the scattering data obtained at 20 °C over the whole q-range. The resulting structural parameters are detailed in Table S1 (ESI†) and the corresponding fit is plotted in Fig. S1 (ESI†).

Comparing to literature values, we focus, in particular, on the lateral area per lipid. From our analysis we obtained $A = 64.3$ Å^2, which agrees favorably with $A = 66.9$ Å^{2}[63] and $A = 67.6$ Å^{2},[31] both obtained at 30 °C, considering the lateral expansion of the bilayer with temperature.[46] We therefore conclude that our model successfully captures high-resolution structural information of single component bilayers also. For further structural results of DOPC, see the ESI.†

4.1 Microscopic domains

The next step was to evaluate the model for micron-sized domains, which have been shown to exhibit long-range out-of-plane domain alignment in multibilayers and which have been analyzed in terms of a global SAXS data analysis before.[27,64] Thus our system of choice was the above detailed mixture of DOPC/DSPC/Chol (0.46/0.3/0.24).[65] The corresponding data shown in Fig. 2 clearly show the presence of two coexisting lamellar lattices, where the higher d-spacing phase (76.7 Å) is ascribed to the L_O-dominated stacks, implying that the lattice of $d = 66.9$ Å corresponds the L_D-dominated stacks. These values are in excellent agreement with our previous report.[27]
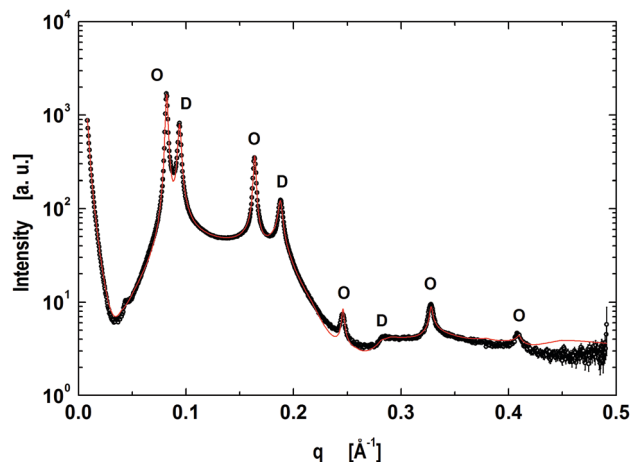

Fig. 2 Global analysis (red line) of microscopically phase separated DOPC/DSPC/Chol multibilayers. Peaks corresponding to L_D dominated stacks are indicated by 'D's' and 'O's' correspond to the lamellar lattice of L_O dominated stacks.

Our model is able to fit the data well up to $q < 0.4$ Å^{-1}. Discrepancies for $q > 0.4$ Å^{-1} are most probably caused by subtle structural features of the L_O polar headgroup region, which we currently do not capture. The resulting group distribution functions of the L_D and L_O phases and the corresponding electron density profiles are presented in Fig. 3.

Lattice parameters obtained from our detailed analysis (Table 1) show that about two thirds of the sample ($l_D = 0.675$) was composed
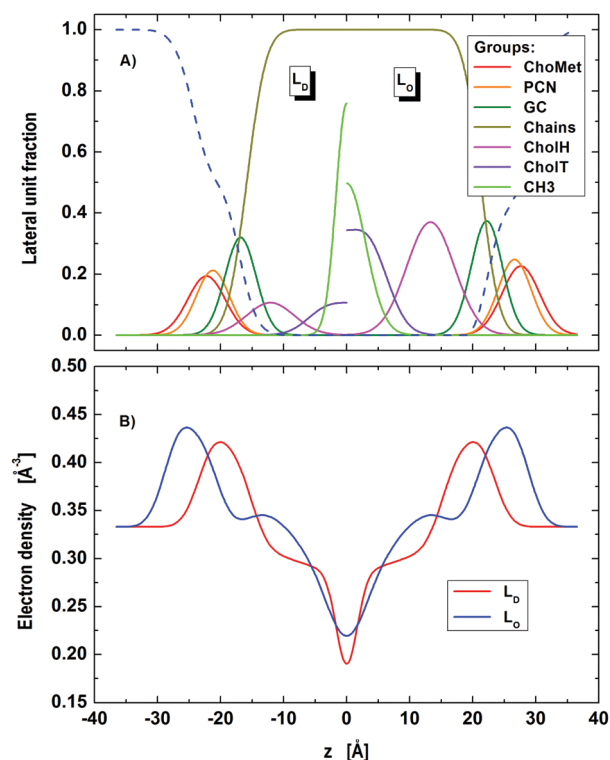

Fig. 3 Distribution of component groups (A) and corresponding electron density profiles (B) of DOPC/DSPC/Chol L_D and L_O domains in the microscopic regime.

Table 1 MLV lattice structure parameters in the microscopic regime. Parameter uncertainties are <2%

Parameter	Bilayer lattice	
	L_D-dominated	L_O-dominated
l_i	0.67	0.33
Φ_i	0.94	0.73
d [Å]	66.9	76.6
$\eta \times 10^{-2}$	13.4	3.3
Δ_{fl} [Å]	7.8	4.5
N_{bil}	10.5	10.9

Table 2 Structural parameters of L_D and L_O domains in the microscopic regime. Parameter uncertainties are <2%

Parameter	Microdomains	
	L_D domains	L_O domains
A [Å^2]	69.5	57.4
A^m [Å^2]	57.5	38.4
D_C [Å]	16.0	21.2
D_B [Å]	41.5	53.9
D_{HH} [Å]	42.6	53.4
z_{GC} [Å]	16.9	22.2
z_{PCN} [Å]	21.3	26.7
$r_{Chol,i}$	0.208	0.493
z_{Chol} [Å]	12.1	13.3
σ_{CH_3} [Å]	1.94	2.63

of L_D dominated stacks. Looking at the abundance of each phase we found that L_D-stacks were somewhat 'purer' in L_D domains (Φ_D = 93.6%) than L_O stacks in L_O domains (Φ_O = 73.1%).

The relative molar ratios of cholesterol were found to be r_O = 0.493 in L_O domains and r_D = 0.208 in L_D domains. These data compare well with r_D = 0.205 and r_O = 0.471 reported for the same tie-line from FRET studies by Heberle et al.,[14] lending strong support to the applied modeling. We emphasize that the obtained results for r_D and r_O were stable without the need to apply constraints.

Bending fluctuations were significantly lower in L_O domains, i.e. by a factor of ~1.75, than in L_D domains. This is consistent with an increased content of DSPC and cholesterol in L_O[65] that leads to an increase in bending rigidity.[66,67] Note, however, that our reported bending fluctuations are a function of bending rigidity and interactions across the aqueous phase (eqn (5)). That is, the decrease of η for L_O domains may also be due to an increase of interactions. This can be illustrated using eqn (5) and assuming that B is equal for both domains. A detailed interaction analysis of the same system using osmotic stress reported that L_O domains are almost three times more rigid than L_D domains.[64] Using this information we then calculate that η for L_D domains should be about two times larger than for L_O domains. However, our experimentally determined η values differ by a factor of four (Table 1), signifying that the smaller fluctuations of L_O domains are partially also due to increased interactions.

Our η values were systematically larger than reported previously.[27] This can be attributed to the presently higher experimental resolution and the improved model description. Interestingly, the bending fluctuations of L_D domains, which are rich in DOPC, are significantly higher (factor: ~2.4) than those of pure DOPC MLVs (see Table S1, ESI†), despite the fact that they contain some cholesterol. This might be due to local bilayer thinning defects at the domain boundaries as suggested by Nickels et al.,[26] leading to increased domain fluctuation amplitudes.

Turning to the domain structure (Table 2) and comparing with our previous report,[27] the new A values are somewhat higher for both domains (L_D: A = 69.5 Å^2 vs. 60.3 Å^2 and L_O: A = 57.4 Å^2 vs. 43.1 Å^2), especially for L_O. We believe, that the discrepancies are mainly caused by different ways of calculating A. Here, we fitted A assuming volume conservation of the hydrocarbon core, considering also the contributions from cholesterol, while Heftberger et al.[27] calculated A by finding the Luzzati thickness from the water distribution function.

Further, the improved quality of data and model fits may also explain the observed differences. The increase of A in L_D domains, with respect to pure DOPC (Table S1, ESI†) is due to the fraction of cholesterol contributing to the unit cell, consistent with a previous report on binary mixtures with cholesterol.[47] Defining the average lateral area per molecule as $A^m = A/n_m$, where n_m is the number of molecules per unit cell (including both PCs and Chol), we find a tighter packing of the molecules in both domains (A_D^m = 57.5 Å^2 vs. A_O^m = 38.4 Å^2) as compared to pure DOPC, which naturally agrees with the commonly accepted lateral membrane condensation property of cholesterol. The lower A-value of L_O domains as compared to L_D domains is consistent with an enrichment in cholesterol and DSPC.

Because D_C is coupled to A (eqn (10)), our hydrocarbon core thickness values are smaller than reported previously (~2 Å for L_D and ~5 Å for L_O).[27] However, when comparing the Luzzati thicknesses, these differences are minimal, in particular for L_O domains (present: $D_B(L_D)$ = 41.5 Å, $D_B(L_O)$ = 53.9 Å; Heftberger et al.:[27] $D_B(L_D)$ = 39.2 Å, $D_B(L_O)$ = 49.2 Å) and almost agree within the experimental resolution.

Finally, the average positions of the cholesterol headgroup were almost identical in both phases, $z_{Chol}(L_D)$ = 12.1 Å and $z_{Chol}(L_O)$ = 13.3 Å, which is in good agreement with our previous report using a simpler parsing description for cholesterol.[27]

4.2 Nanoscopic domains

Nanoscopic domains in POPC/DSPC/Chol (0.39/0.39/0.22), did not exhibit long-range out-of-plane positional correlations of like domains, but displayed only a single lamellar lattice (Fig. 4) with a d-value of 75.9 Å, i.e. very close to the d of micron-sized L_O domains (Table 1). To exclude the possibility of the randomly-mixed bilayers, we also carried out a corresponding single phase fit. However, even the best single phase fit, for which we also tried to release some of the volumetric constraints, was not able to follow the scattering curve (Fig. 4). In particular, the homogeneous model fails to account for the observation that minima of the scattered intensity are not on the same level. This is due to the fact that the form factor of a homogeneous bilayer needs to pass through zero, which is not necessarily the case for a heterogeneous bilayer with a mixed form factor (see, e.g., eqn (15)–(18)). Note, however,
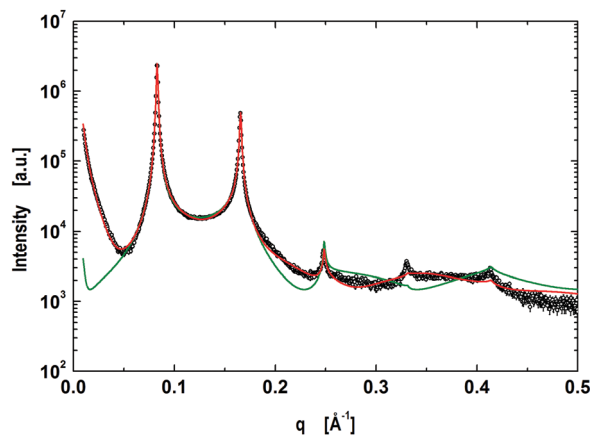
Fig. 4 Global analysis (red line) of coexisting nanoscopic domains in POPC/DSPC/Chol multibilayers. The green line shows the best fit assuming homogeneous lipid mixing.

that we have demonstrated previously, that non-phase-separated mixtures of phospholipids with cholesterol are well-described by a homogeneous model.[27,31] This encouraged us to utilize the model for coexisting nanoscopic domains.

During fitting with the nanoscopic domain model, we found instabilities of the optimization primarily in cholesterol related parameters (position, concentration). This is most likely due to the small contrast between nanoscopic L_O and L_D domains for X-rays. Further exploitation of this issue requires a joint analysis of differently contrasted SANS data with the SAXS data of nanoscopic domains. Such studies are currently being planned in our laboratory. Note that the presently described analysis is capable of performing this analysis without any further modification. To analyze current SAXS data, we tested different sets of different structural and volumetric constraints for cholesterol. The best stable fit was obtained upon fixing (i) the relative cholesterol molar ratios ($r_D = 0.14$, $r_O = 0.34$) according to reported tie-line endpoints of the same mixture,[65] (ii) the relative positions of cholesterol to GC-groups, $\Delta z_{Chol,i} = z_{GC,i} - z_{Chol,i}$, to the values obtained in the microscopic regime ($\Delta z_{Chol,D} = 4.8$ Å, $\Delta z_{Chol,O} = 8.9$ Å), and (iii) the cholesterol molecular volumes ($V_{Chol,D} = V_{Chol,O} = 630$ Å^3) in agreement with the results obtained by Heberle *et al.*[65] The resulting fit and domain structure are shown in Fig. 4 and 5, the corresponding model parameters are summarized in Tables 3 and 4.

Regarding the lattice parameters (Table 3) we found that the bending fluctuations, η, and their amplitudes, Δ_{fl}, are close to those in micron-sized L_O domains. This is consistent with L_D domains being less abundant than L_O domains, as obtained from our analysis ($\Phi_D = 32\%$). The latter value is also in agreement with the reported compositional phase diagram.[14] Interestingly, the found fraction of leaflet anti-correlated domains is small ($\Phi_A \sim 1\%$). Nevertheless, Φ_A has a significant effect on the scattered intensity. That is, setting $\Phi_A = 0$ does not produce a satisfactory fit of the SAXS pattern.

The observation of only a single lattice might also be connected to the beam's coherence length, ξ. In general ξ is a function of the beamline geometry (transversal coherence
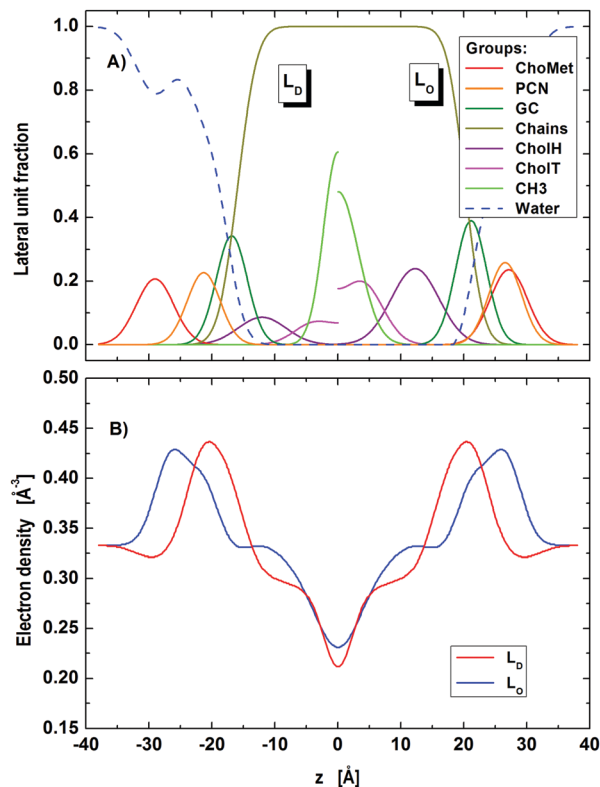

Fig. 5 Distribution of component groups (A) and corresponding electron density profiles (B) of POPC/DSPC/Chol L_D and L_O domains in the nanoscopic regime.

Table 3 MLV lattice structure parameters in the nanoscopic regime. Parameter uncertainties are <2%

Parameter	Bilayer lattice
Φ_D	0.32
Φ_A	0.023
d [Å]	75.9
$\eta \times 10^{-2}$	4.9
Δ_{fl} [Å]	5.3
N_{bil}	16.8

Table 4 Structural parameters of L_D and L_O domains in the nanoscopic regime. Parameter uncertainties are <2%

Parameter	Nanodomains	
	L_D domains	L_O domains
A [Å^2]	64.1	56.3
A^m [Å^2]	56.2	42.0
D_C [Å]	15.9	20.2
D_B [Å]	42.2	52.1
D_{HH} [Å]	42.6	53.1
z_{GC} [Å]	16.9	21.1
z_{PCN} [Å]	21.3	26.5
$r_{Chol,i}^a$	0.14	0.34
z_{Chol}^a [Å]	12.1	12.3
σ_{CH_3} [Å]	2.3	3.2

^{a} Fixed values.

length) and the energy bandwidth (longitudinal coherence length).[16,68] Specifically, ξ influences the weight given to the

scattering of the individual lattices of 'pure' like domains and their cross interference. That is, 'pure' terms become dominant if the characteristic length of positional correlations of like domains is on the order of ξ (or larger). In this case, we would observe two lattices as in the case of micron-sized domains. Likewise, interference term(s) become dominant, if the characteristic length of positional correlations of domains is significantly smaller than ξ. Typical coherence lengths at synchrotron sources are on the order of a few microns. Thus, the single d-value found for nanoscopic domains could well be related to this effect. However, these considerations require that the two lattices have distinct d-values. We are currently not able to discern the different possible organizations of nanoscopic domains. Neutron diffraction experiments, analogous to those performed on dipalmityol phosphatidylcholine bilayers in the phase transition region[68] might be useful to shed some light on this issue.

Regarding the domain structure, we did also observe changes compared to micron-sized domains (Table 4; for corresponding electron densities and component distribution functions, see Fig. 5). For example, the area per lipid of L_D domains reduced by about 7%, while A_O decreased by about 2% only. That is, the mismatch in the packing of lipids between L_D and L_O, $\Delta A = |A_D - A_O|$ domains becomes much less expressed for nanoscopic domains ($\Delta A^{nano} \sim 8$ Å^2, $\Delta A^{micro} \sim 12$ Å^2). This may at least in part be due to the different composition of the presently studied nanoscopic L_D domains, which with POPC as the dominant species contain a lipid that has a smaller area per lipid than DOPC, enriched in 'our' micron-sized L_D domains.[46,69]

Focusing on the transdomain structure, we see the strongest changes to be a decrease in D_C by ~ 1.0 Å and in D_B by ~ 1.8 Å for L_O domains, whereas the thickness changes in L_D were significantly smaller. This yields in total a smaller thickness difference between the L_O and L_D domains ($\Delta D_B = D_B(L_O) - D_B(L_D)$) in the nanoscopic regime, when compared to the microscopic one ($\Delta D_B^{nano} \sim 10$ Å, $\Delta D_B^{micro} \sim 12$ Å), which is consistent with a previous report.[22] Differences to previously reported absolute values of D_B[22,26] may be due to different model descriptions for the scattering length densities.

5 Conclusions

In the present paper, we have advanced our previously reported SDP model[27] for *in situ* studies of coexisting lipid domains in multibilayers. The presented model accounts for defects induced by positionally anticorrelated domains in micron-sized domains coexisting in MLVs. For nanoscopic domains, no long-range alignment of like domains along the stacking direction was observed. However, modeling had to account for contributions from overlapping/asymmetric domains (L_D/L_O, L_O/L_D), which was inspired by a recent simulation report.[45] Our modeling allowed us to capture a range of structural details, *e.g.* area per unit cell, domain thickness, *etc.*, of coexisting microscopic and nanoscopic domains. We note that the here presented model does not capture in-plane scattering of domains. Such scattering is expected to occur at very low q-ranges and has been observed previously using

SANS in combination with contrast variation.[22] SAXS is rather insensitive to in-plane domain scattering, which allowed us to neglect this contribution.

We found distinct differences in lipid packing densities and domain thicknesses in micron-sized domains in agreement with previous results.[27] These differences were found to be less expressed for nano-sized lipid domains, signifying a decrease of thickness mismatch between L_D and L_O, in agreement with a previous neutron scattering study.[22] Here, we also found that the packing of lipids becomes more alike, in particular by laterally more condensed nanoscopic L_D domains. For micron-sized domains, our analysis allowed us to determine cholesterol partitioning in L_O and L_D phases, which agreed well with published data from compositional phase diagrams.

We emphasize that deriving these structural details did neither involve the use of any labels, nor require measuring samples at tieline endpoints. Future studies will be extended to an SDP-based joint neutron and X-ray data analysis to fully exploit contrast variation, analogous to several previous reports on homogeneous lipid bilayers systems.[16,70] This will allow us to test the results obtained from current modeling and enable us to determine cholesterol content in nanoscopic domains.

References

1 K. Gaus, E. Gratton, E. P. W. Kable, A. S. Jones, I. Gelissen, L. Kritharides and W. Jessup, *Proc. Natl. Acad. Sci. U. S. A.*, 2003, **100**, 15554–15559.

2 T. Baumgart, A. T. Hammond, P. Sengupta, S. T. Hess, D. A. Holowka, B. A. Baird and W. W. Webb, *Proc. Natl. Acad. Sci. U. S. A.*, 2007, **104**, 3165–3170.

3 D. Lingwood, J. Ries, P. Schwille and K. Simons, *Proc. Natl. Acad. Sci. U. S. A.*, 2008, **105**, 10005–10010.

4 K. Jacobson, O. G. Mouritsen and R. G. W. Anderson, *Nat. Cell Biol.*, 2007, **9**, 7–14.

5 K. Simons and D. Toomre, *Nat. Rev. Mol. Cell Biol.*, 2000, **1**, 31–39.

6 D. Lingwood and K. Simons, *Science*, 2010, **327**, 46–50.

7 M. L. Kraft, *Mol. Biol. Cell*, 2013, **24**, 2765–2768.

8 E. Sevcsik, M. Brameshuber, M. Fölser, J. Weghuber, A. Honigmann and G. J. Schütz, *Nat. Commun.*, 2015, **6**, 6969.

9 L. J. Pike, *J. Lipid Res.*, 2006, **47**, 1597–1598.

10 D. Marsh, *Biochim. Biophys. Acta, Biomembr.*, 2009, **1788**, 2114–2123.

11 H. M. McConnell and A. Radhakrishnan, *Biochim. Biophys. Acta, Biomembr.*, 2003, **1610**, 159–173.

12 S. A. Pandit, D. Bostick and M. L. Berkowitz, *Biophys. J.*, 2004, **86**, 1345–1356.

13 L. A. Bagatolli and E. Gratton, *Biophys. J.*, 2000, **78**, 290–305.

14 F. A. Heberle, J. Wu, S. L. Goh, R. S. Petruzielo and G. W. Feigenson, *Biophys. J.*, 2010, **99**, 3309–3318.

15 C. L. Armstrong, D. Marquardt, H. Dies, N. Kučerka, Z. Yamani, T. A. Harroun, J. Katsaras, A.-C. Shi and M. C. Rheinstädter, *PLoS One*, 2013, **8**, e66162.

16 D. Marquardt, F. A. Heberle, J. D. Nickels, G. Pabst and J. Katsaras, *Soft Matter*, 2015, **11**, 9055–9072.

17 S. L. Veatch, I. V. Polozov, K. Gawrisch and S. L. Keller, *Biophys. J.*, 2004, **86**, 2910–2922.

18 M. Gandhavadi, D. Allende, A. Vidal, S. Simon and T. McIntosh, *Biophys. J.*, 2002, **82**, 1469–1482.

19 M. Frewein, B. Kollmitzer, P. Heftberger and G. Pabst, *Soft Matter*, 2016, **12**, 3189–3195.

20 G. W. Feigenson, *Biochim. Biophys. Acta, Biomembr.*, 2009, **1788**, 47–52.

21 S. L. Veatch, K. Gawrisch and S. L. Keller, *Biophys. J.*, 2006, **90**, 4428–4436.

22 F. A. Heberle, M. Doktorova, S. L. Goh, R. F. Standaert, J. Katsaras and G. W. Feigenson, *J. Am. Chem. Soc.*, 2013, **135**, 14932–14935.

23 I. V. Ionova, V. A. Livshits and D. Marsh, *Biophys. J.*, 2012, **102**, 1856–1865.

24 T. M. Konyakhina, J. Wu, J. D. Mastroianni, F. A. Heberle and G. W. Feigenson, *Biochim. Biophys. Acta, Biomembr.*, 2013, **1828**, 2204–2214.

25 M. Schick, *Phys. Rev. E: Stat., Nonlinear, Soft Matter Phys.*, 2012, **85**, 031902.

26 J. D. Nickels, X. Cheng, B. Mostofian, C. Stanley, B. Lindner, F. A. Heberle, S. Perticaroli, M. Feygenson, T. Egami, R. F. Standaert, J. C. Smith, D. A. A. Myles, M. Ohl and J. Katsaras, *J. Am. Chem. Soc.*, 2015, **137**, 15772–15780.

27 P. Heftberger, B. Kollmitzer, A. A. Rieder, H. Amenitsch and G. Pabst, *Biophys. J.*, 2015, **108**, 854–862.

28 R. Zhang, R. M. Suter and J. F. Nagle, *Phys. Rev. E: Stat. Phys., Plasmas, Fluids, Relat. Interdiscip. Top.*, 1994, **50**, 5047–5060.

29 N. Kučerka, J. F. Nagle, J. N. Sachs, S. E. Feller, J. Pencer, A. Jackson and J. Katsaras, *Biophys. J.*, 2008, **95**, 2356–2367.

30 L. Chen, Z. Yu and P. J. Quinn, *Biochim. Biophys. Acta, Biomembr.*, 2007, **1768**, 2873–2881.

31 P. Heftberger, B. Kollmitzer, F. A. Heberle, J. Pan, M. Rappolt, H. Amenitsch, N. Kučerka, J. Katsaras and G. Pabst, *J. Appl. Crystallogr.*, 2014, **47**, 173–180.

32 G. Pabst, M. Rappolt, H. Amenitsch and P. Laggner, *Phys. Rev. E: Stat. Phys., Plasmas, Fluids, Relat. Interdiscip. Top.*, 2000, **62**, 4000–4009.

33 G. Pabst, R. Koschuch, B. Pozo-Navas, M. Rappolt, K. Lohner and P. Laggner, *J. Appl. Crystallogr.*, 2003, **36**, 1378–1388.

34 S. Karmakar, B. Sarangi and V. Raghunathan, *Solid State Commun.*, 2006, **139**, 630–634.

35 L. Tayebi, Y. Ma, D. Vashaee, G. Chen, S. K. Sinha and A. N. Parikh, *Nat. Mater.*, 2012, 1074–1080.

36 A. Guinier, *X-ray Diffraction*, W. H. Freeman & Co., San Francisco, 1963.

37 R. Zhang, S. Tristram-Nagle, W. Sun, R. L. Headrick, T. C. Irving, R. M. Suter and J. F. Nagle, *Biophys. J.*, 1996, **70**, 349–357.

38 P. G. de Gennes and J. Prost, *The Physics of Liquid Crystals*, Oxford University Press, Oxford, New York, 2nd edn, 1993.

39 H. I. Petrache, PhD thesis, Carnegie Mellon University, Pensilvania, USA, 1998.

40 T. Frühwirth, G. Fritz, N. Freiberger and O. Glatter, *J. Appl. Crystallogr.*, 2004, **37**, 703–710.

41 S. R. Aragon and R. Pecora, *J. Chem. Phys.*, 1976, **64**, 2395.

42 P. Bartlett and R. H. Ottewill, *J. Chem. Phys.*, 1992, **96**, 3306.

43 J. Pencer, S. Krueger, C. P. Adams and J. Katsaras, *J. Appl. Crystallogr.*, 2006, **39**, 293–303.

44 M. C. Blosser, A. R. Honerkamp-Smith, T. Han, M. Haataja and S. L. Keller, *Biophys. J.*, 2015, **109**, 2317–2327.

45 P. W. Fowler, J. J. Williamson, M. S. P. Sansom and P. D. Olmsted, *J. Am. Chem. Soc.*, 2016, 11633–11642.

46 N. Kučerka, M.-P. Nieh and J. Katsaras, *Biochim. Biophys. Acta*, 2011, **1808**, 2761–2771.

47 N. Kučerka, J. Pencer, M.-P. Nieh and J. Katsaras, *Eur. Phys. J. E: Soft Matter Biol. Phys.*, 2007, **23**, 247–254.

48 O. Edholm and J. F. Nagle, *Biophys. J.*, 2005, **89**, 1827–1832.

49 A. Hodzic, M. Rappolt, H. Amenitsch, P. Laggner and G. Pabst, *Biophys. J.*, 2008, **94**, 3935–3944.

50 D. Marsh, *Handbook of Lipid Bilayers*, CRC Press, Boca Raton, 2nd edn, 2013.

51 J. B. Klauda, N. Kučerka, B. R. Brooks, R. W. Pastor and J. F. Nagle, *Biophys. J.*, 2006, **90**, 2796–2807.

52 D. Uhríková, P. Rybár, T. Hianik and P. Balgavý, *Chem. Phys. Lipids*, 2007, **145**, 97–105.

53 Y. Ma, S. K. Ghosh, D. A. DiLena, S. Bera, L. B. Lurio, A. N. Parikh and S. K. Sinha, *Biophys. J.*, 2016, **110**, 1355–1366.

54 J. Gallová, M. Klacsová, F. Devnsky and P. Balgavý, *Chem. Phys. Lipids*, 2015, **190**, 1–8.

55 P. Heftberger, PhD thesis, Technische Universität Graz, Graz, 2015.

56 J. F. Nagle and S. Tristram-Nagle, *Biochim. Biophys. Acta*, 2000, **1469**, 159–195.

57 A. A. Rieder, D. Koller, K. Lohner and G. Pabst, *Chem. Phys. Lipids*, 2015, **186**, 39–44.

58 P. B. Kingsley and G. W. Feigenson, *Chem. Phys. Lipids*, 1979, **24**, 135–147.

59 P. Pernot, A. Round, R. Barrett, A. De Maria Antolinos, A. Gobbo, E. Gordon, J. Huet, J. Kieffer, M. Lentini, M. Mattenet, C. Morawe, C. Mueller-Dieckmann, S. Ohlsson, W. Schmid, J. Surr, P. Theveneau, L. Zerrad and S. McSweeney, *J. Synchrotron Radiat.*, 2013, **20**, 660–664.

60 C. E. Blanchet, A. Spilotros, F. Schwemmer, M. A. Graewert, A. Kikhney, C. M. Jeffries, D. Franke, D. Mark, R. Zengerle, F. Cipriani, S. Fiedler, M. Roessle and D. I. Svergun, *J. Appl. Crystallogr.*, 2015, **48**, 431–443.

61 M. V. Petoukhov, D. Franke, A. V. Shkumatov, G. Tria, A. G. Kikhney, M. Gajda, C. Gorba, H. D. T. Mertens, P. V. Konarev and D. I. Svergun, *J. Appl. Crystallogr.*, 2012, **45**, 342–350.

62 R. Storn and K. Price, *J. Global Optim.*, 1997, **11**, 341–359.

63 N. Kučerka, S. Tristram-Nagle and J. F. Nagle, *J. Membr. Biol.*, 2006, **208**, 193–202.

64 B. Kollmitzer, P. Heftberger, R. Podgornik, J. F. Nagle and G. Pabst, *Biophys. J.*, 2015, **108**, 2833–2842.

65 F. A. Heberle, R. S. Petruzielo, J. Pan, P. Drazba, N. Kučerka, R. F. Standaert, G. W. Feigenson and J. Katsaras, *J. Am. Chem. Soc.*, 2013, **135**, 6853–6859.

66 D. Needham and R. Nunn, *Biophys. J.*, 1990, **58**, 997–1009.

67 W. Rawicz, K. Olbrich, T. McIntosh, D. Needham and E. Evans, *Biophys. J.*, 2000, **79**, 328–339.

68 C. L. Armstrong, M. A. Barrett, L. Toppozini, N. Kučerka, Z. Yamani, J. Katsaras, G. Fragneto and M. C. Rheinstädter, *Soft Matter*, 2012, **8**, 4687.

69 N. Kučerka, J. Gallová, D. Uhríková, P. Balgavý, M. Bulacu, S.-J. Marrink and J. Katsaras, *Biophys. J.*, 2009, **97**, 1926–1932.

70 G. Pabst, N. Kučerka, M.-P. Nieh, M. Rheinstädter and J. Katsaras, *Chem. Phys. Lipids*, 2010, **163**, 460–479.